A numerical and experimental identification of crystallinity gradients in carbon fiber reinforced thermoplastic composites obtained by laser assisted filament winding

Anna Maria El Bayssari, Mael Péron, Anaïs Barasinski, Frédéric Jacquemin, Federica Daghia, Damien Guillon

A numerical and experimental identification of crystallinity gradients in carbon fiber reinforced thermoplastic composites obtained by laser assisted filament winding

Anna Maria El Bayssari [1], Mael Péron[2,*], Anaïs Barasinski[1], Frédéric Jacquemin[2], Federica Daghia[3], Damien Guillon[4]

[1]Université de Pau et des Pays de l'Adour, E2S UPPA, CNRS, IPREM, 64000 Pau, France
[2] Nantes Université, Ecole Centrale de Nantes, CNRS, GeM, UMR CNRS 6183, F-44600 Saint-Nazaire, France
[3] Université Paris-Saclay, CentraleSupélec, ENS Paris-Saclay, CNRS, LMPS - Laboratoire de Mécanique Paris-Saclay, 91190, Gif-sur-Yvette, France.

[4]Cetim, Centre technique des industries mécaniques, Nantes, France

* Corresponding author (mael.peron@univ-nantes.fr)

Keywords: Thermoplastic, Thermal Modelling, Crystallinity gradients, Laser assisted filament winding

Abstract

The presence of temperature and crystallinity gradients in carbon fiber–reinforced PolyEtherEtherKetone (PEEK) composite laminates, produced via laser-assisted tape placement, is investigated in this paper. The manufacturing process takes place with high deposition speed and using localized laser source for heating, therefore enhancing the formation of temperature and crystallinity gradients through the laminate thickness. A previously validated thermal model coupled with a non-isothermal crystallinity model and a fusion model are used to simulate the temperature and crystallinity distributions through the laminate thickness. The results from the model are correlated with Dynamic Mechanical Analysis (DMA) tests and Differential Scanning Calorimetry (DSC) tests since a crystallinity gradient is difficult to monitor experimentally. The simulated gradients suggested the presence of an amorphous layer between two consecutive plies and an increase in the crystallinity through the material's thickness. This observation is correlated with the behavior reported for the semi-crystalline laminates during the DMA test, where the modulus drops abruptly during the glass transition, a typical behavior for an amorphous material.

1 Introduction

Automated manufacturing techniques with in-situ consolidation such as filament winding and tape placement have been widely studied recently [1,2]. The growing interest resulted from the several advantages of the automation such as the increase of the production rate, decrease of the labor cost and repeatability over the produced parts. In-situ consolidation during these automated processes relies on a local heating of the prepreg tape and the upper surface of the substrate while applying a local pressure via a compaction roller. Despite the multiple advantages of the automated filament winding and tape placement processes [1,2], these processes are yet to be widely applied. Indeed, several aspects of the processes need to be further explored. For instance, the in-situ consolidation with local heating (*e.g.* laser heating) are associated with thermal gradients through the thickness [3–6]. One of the main issues related to the thermal gradients is the occurrence of complex crystallinity gradients through the laminate thickness. These crystallinity gradients affect the composite material subsequent properties and its consolidation [7] and therefore need to be studied. A number of numerical and analytical works dealt with the evolution of the crystallinity during the tape placement and filament winding. Mantel and Springer [8] studied the

crystallization behavior of APC-2 during tape placement using Lee and Springer's model [9] and the model of Velisaris and Seferis [10]. Nejhad et al. [11] also used the model developed by Velisaris and Seferis [10] to study the evolution of crystallinity during filament winding of APC-2 prepreg. The results showed a crystallinity gradient through the laminate thickness. However, no experimental validation was conducted to validate the crystallinity model applied. Tierney and Gillespie [12] implemented the same model considered by Mantell and Springer [8] with the same parameters for a single ply heated with a gas torch. Sonmez and Hahn in [6] used the model developed in [13] during the cooling phase of an automated tape placement process to simulate the crystallization of PEEK/AS4 composite. They were also the only ones to incorporate the fusion model of Maffezolli et al. [14] to calculate the residual degree of crystallinity during tape placement of APC-2 composite. A review of the key studies can be found in [15]. These studies dealt with the experimental characterization of the thermal gradients which might ultimately lead to crystallinity gradients. Some works tried to simulate the presence of these crystallinity gradients. However, the experimental validation wasn't carried out in the mentioned studies.

As can be seen from the literature review, several studies have pointed out the possible presence of crystallinity gradients through the thickness of composite parts obtained through laser assisted tape placement. However, none of them have validated this experimentally, as was concluded in [15]. In the present study, a laser assisted filament winding machine called SPIDE-TP was used to produce several laminates in CETIM in Nantes, France. Specimen selected from the laminates are subjected to Differential Scanning Calorimetry (DSC) scans to evaluate the mean crystallinity and transition temperatures of the material just after the processing. In parallel, Dynamic Mechanical Analysis (DMA) tests are performed together with standard three-point bending tests in order to monitor the evolution of the material stiffness with temperature and to identify the glass transition temperature after the process, but also after an annealing at 250°C. Results from both experimental methods are compared and discussed. Finally, a multi-physical model including heat transfer, crystallization and fusion of the PEEK matrix is proposed to predict the thermal history and crystallization distribution within the material during processing. Results from this model are finally compared with the experimental results obtained by DSC.

2 Experimental characterization

2.1 Materials

The composite material selected for this study is the PEEK/AS4 from Tencate Cetex®, commercially known as APC-2 (Aromatic Polymer Composite). It is provided in the form of pre-impregnated tapes with a width, thickness and volumetric fiber fraction around 6.35 mm, 0.15 mm and 59% respectively according to the manufacturer. The APC-2 is a high-performance composite with thermoplastic PEEK with a grade 150G.

2.2 Processing and sample preparation

The tapes were processed on the SPIDE-TP, a laser-assisted filament winding machine based in CETIM in Nantes, France. SPIDE-TP is composed of a 6-axis universal Kuka Robot together with 3 additional mechanical axes. It includes two winding axes which allow the manufacturing of revolution parts with various sizes (from 10 mm to 2.5 m in diameter and up to 6 m in length) and one central axis that allows the displacement of the deposition head in a direction parallel to the winding axis. The robot is equipped with a dispensing head provided by AFPT GmbH. This tape placement head is equipped with a near-infrared (NIR) 4kW diode laser with a wavelength range from 940 to 1070 nm from Laserline GmbH. The laser beam is focused with a lens that lead to a 20 mm width by 40 mm high rectangular spot at a distance of 270

mm from the lens. The focal plane is located around the nip-point. The incoming thermoplastic tape is fed and guided through the deposition head with a defined tension. It receives irradiation from the laser and rapidly heats up before being compacted on the substrate by a silicone consolidation roller.

The temperature of the heating zone on both the tape and the substrate is monitored with a FLIR T660 infrared camera. The SPIDE-TP system adjusts the laser power and angle in order that both apparent temperature of the tape and substrate reach the targeted value.

6 and 9-plies UD laminates were chosen for this study in order to study the transverse behavior directly related to the resin's crystallinity. The choice of stacking sequences was made as a compromise between having sufficient number of plies to avoid any boundary effect and reducing the number of plies needed. The tapes are continuously laid by a placement head on a cold mandrel at ambient temperature while heated with the laser source during their deposition to ensure their melting. Following the heating step, a silicone roller applies a pressure on the surface of the deposited plies to ensure the compaction of the structure.

The laminates were processed with a deposition speed v_{dep}=0.15 m/s and a nip-point temperature $T_{nip-point}$ maintained at 410°C. As mentioned previously, the laser power is not a user selected parameter but is automatically adjusted via the SPIDE-TP to maintain the nip-point temperature selected at 410°C. This temperature was obtained with a mean laser power value of 1000W.

From each UD plate, three rectangular specimens were cut for DMA analysis, four rectangular specimens for quasi-static three-point bending tests and four specimens for the DSC analysis. The different specimens for mechanical testing were cut using a MAC ALISTER® MTC750L cutter equipped with a diamond blade cutter and polished on a Struers® TegraForce-5 polisher using several glass sandpapers starting from big grit size of P320 down to the small grit size of P4000 to ensure a homogeneous section across their length. The specimens' dimensions for the DMA tests and the three-point bending tests are presented in **Table 1** and in **Table 2**, respectively. The three-point bending test specimens were prepared so as to match the standard ISO 14125. For the DSC measurements, the specimens weighed between 5 and 14 mg, and were placed each in a sealed aluminum pan. The thickness of each specimen presents the whole thickness of the laminate from which it was extracted.

Ply sequence	**Specimens number**	**Length between spans or free-length L_0(mm)**	**Width b (mm)**	**Thickness h (mm)**
$[90_6]$	3	20	10±0.02	1 ±0.09
$[90_9]$	3	30	15±0.02	1.3±0.05

Table 1 *- Dimensions of the specimens selected for the three-point bending tests on the DMA machine.*

Ply sequence	**Thickness h (mm)**	**Width b (mm)**	**Span length L_0 (mm)**	**Specimen length L (mm)**
$[90_6]$	1 ±0.1	9.2 ± 0.3	30	45
$[90_9]$	1.4 ±0.1	8.6 ± 0.2	30	45

Table 2 *- Dimensions of the specimens selected for the three-point bending tests on the Instron 3369 machine.*

2.3 Differential scanning calorimetry 'DSC'

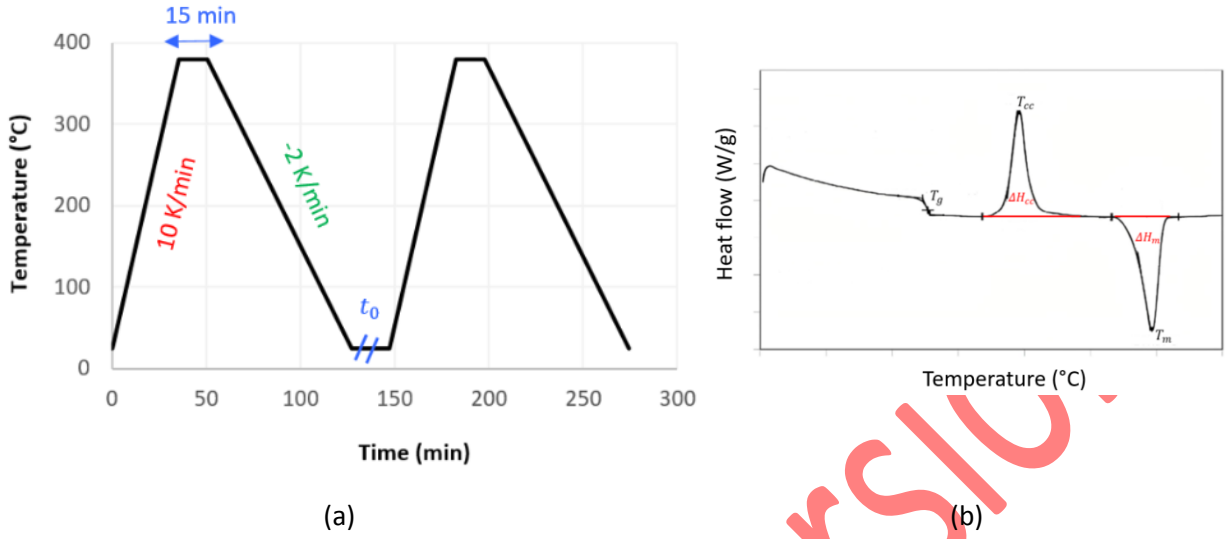

(a) (b)

Figure 1 – *(a) Thermal load applied to the specimens tested under DSC & (b) Determination of the transition temperatures and enthalpies detected during the heating ramp of a thermoplastic resin.*

The DSC used in this work is a Q200 Differential Scanning Calorimeter by TA Instruments®. During the tests, the specimens were heated from room temperature at 25°C until 380°C at a heating rate of 10 K/min as shown in **Figure 1-(a).** They were maintained for 15 mins at 380°C to erase their thermal history and then cooled from 380°C to 25°C at -2 K/min. From this first heating run, the process effect on the produced laminates can be understood. Heating at a constant rate allows the determination of the glass transition T_g , melting temperature T_m and crystallization temperature T_c as shown in **Figure 1**–(b). In order to test the effect of the slow cooling from the melt on the different characteristics studied, the thermal cycle is applied to the same sample a second time.

T_g, T_m and T_c can be directly obtained from the Advantage software provided by TA Instrument with the Q200 DSC by identifying the inflection in the measured flux due to the glass transition, the heat flux maximum peak due to crystallization and the heat flux minimum peak due to fusion, respectively. Thermoplastic polymers can crystallize either during cooling from the melt (hot crystallization) or upon heating from the solid glassy state (cold crystallization). Therefore, the crystallinity fraction χ_c (%) is calculated from the heating scan part of the thermogram by using Equation (1) [16].

$$\chi_c = \frac{\Delta H_m - \Delta H_{cc}}{C_m \Delta H_m^{100}} \times 100 \qquad (1)$$

ΔH_m and ΔH_{cc} are respectively the melting enthalpy (J/g) and the cold crystallization enthalpy (J/g) obtained from the DSC heating scan. ΔH_m^{100} is the theoretical melting enthalpy of a fully crystallized PEEK estimated to be 130 J/g [16] and C_m is the PEEK mass fraction. The cold crystallization enthalpy may not exist whenever the material tested has already reached its maximum crystallinity and, in this case, ΔH_{cc} is equal to zero. The enthalpies corresponding to the melting and cold crystallization correspond to the area under the peaks corresponding to the integral of the heat flow function of time using Equation (2).

$$\Delta H = \int_0^t \frac{\partial H}{\partial t} dt \qquad (2)$$

2.4 Dynamic mechanical analysis 'DMA'

A METTLER TOLEDO® DMA 1 was used for the DMA runs. The storage modulus E' and damping factor tan δ were measured by the three-point bending test. The specimens were subjected to a heating from 25 to 250°C at a rate of 2 K/min and then maintained at 250°C for 10 minutes before starting to cool down. Once cooled down, the specimen which were therefore annealed were subjected to a second heating with the same conditions in order to understand the effect of the annealing at 250°C on the studied characteristics. The tests were performed at a frequency of 1 Hz and a maximum deflection of 10 µm was imposed to remain in the linear elastic domain. The variation of the transverse storage modulus E_{22} and the damping factor $tan\ \delta$ with temperature were directly obtained from the DMA test modulus.

2.5 Static three-point bending tests

The quasi-static three-point bending tests were carried along the transverse direction to measure the transverse modulus, similarly to the DMA tests, on an INSTRON® 3369 machine for which the maximum capacity is 10 kN c.f. **Figure 2**. The samples were loaded with a constant displacement rate fixed at 5 mm/min according to the ISO 14125 standard [17].

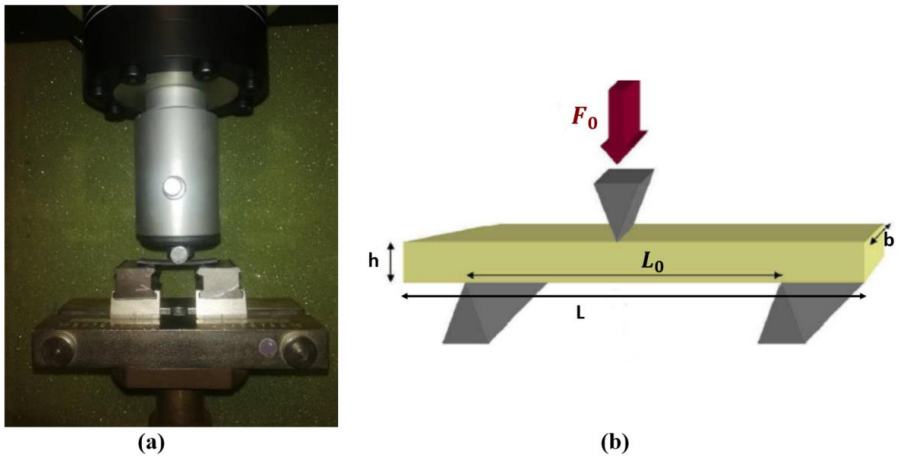

***Figure 2** - (a) Photo of a specimen during a three-point bending test on the Instron 3369 machine (b) - Schematic presentation of the three-point test and the specimens' dimensions.*

A number of specimens were subjected to a static three-point bending machine at ambient temperature. In fact, DMA provides a qualitative presentation of the dependence of the modulus with the temperature. However, the value of the provided modulus can be subjected to errors due to several criteria including uncertainties on the sample dimensions and the stiffness of the DMA machine close to that of the specimen, therefore causing erroneous values. One therefore has to normalize the evolution of the modulus obtained through DMA with the modulus measured at 25°C by standard three-point bending tests.

The control and acquisition during the tests were performed via Bluehill® software connected to an Instron® machine. The software provides a load-displacement curve at the end of each test. To calculate the flexural modulus $E_{flexural}$, the deflections s' and s'' corresponding to the flexural strain $\varepsilon'_{flexural} = 0.05$ % and $\varepsilon''_{flexural} = 0.25\%$ respectively are measured according to the standard ISO 14125 [17] using Equation (3).

$$s = \frac{\varepsilon_{flexural} \times L_0^2}{6h} \quad (3)$$

Once the two deflections s' and s'' are calculated and their corresponding loads identified, $E_{flexural}$ can be calculated using Equation (4).

$$E_{flexural} = \frac{{L_0}^3}{4bh^3}\left(\frac{\Delta F}{\Delta s}\right) \quad (4)$$

ΔF and Δs correspond to the difference between the loads (for ΔF) and mid-point displacement (for Δs) between the loads and displacements corresponding to the flexural strains of 0.05% and 0.25% [17].

3 Experimental results and discussion

3.1 DSC results

Figure 3-(a) & (b) present DSC scans for 6 and 9 plies UD specimens respectively. The trends in **Figure 3** are the same for the rest of the specimens. The behavior of the material after the process can be studied during this heating run. An exothermic peak at 173°C (**Figure 3**) indicates the occurrence of a cold crystallization. An endothermic peak characteristic of the melting of the crystalline phase within the composite is detected at 345°C for both cases**.** It translates the breaking of covalent bonds and the melting of the crystals. The difference between the exothermic and endothermic peaks suggests the presence of partially crystallized regions in the material after processing on the SPIDE-TP and prior to the DSC tests. In contrast to the 1st heating, no exothermic peak is detected upon heating the specimen a second time. It can be concluded that the specimen was able to fully crystallize during its slow cooling from the melt in the DSC.

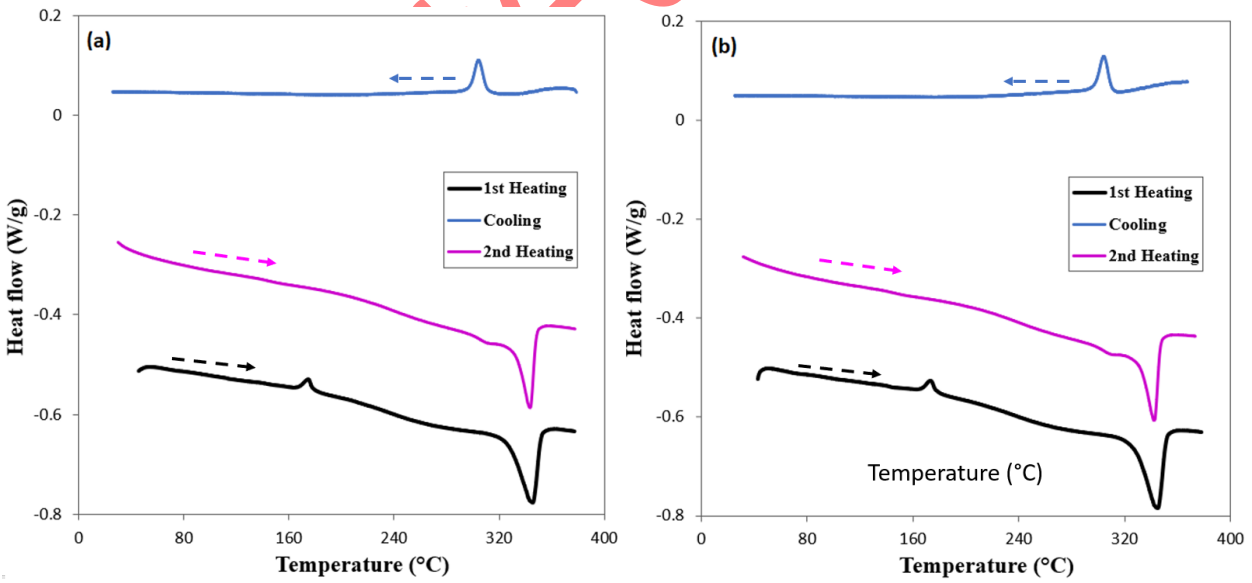

Figure 3 *- DSC thermogram obtained for the 6 (a) and 9 (b) plies specimens.*

3.1.1 Crystallinity fraction

1st Heating

The crystallinity resulting from the process is estimated during the 1st heating and is equal to 23.5 ±0.3% and 21.4±0.2% for the 6-plies and 9-plies UD laminates respectively. These measured values are lower than the ones reported in the literature for PEEK/AS4 composites, which attain 34% according to [18]. In order to understand the origin of such a difference, the factors influencing the crystallinity fraction should be addressed. In fact, an important factor influencing the crystallinity fraction is the cooling rate. This dependency was previously studied by several authors [18–20] and a summary of the values reported in the literature are presented in **Figure 4**. The different works reported show a decrease in the crystallinity fraction when the cooling rate increases. The results presented in **Figure 4** are scattered due to either the type of resin and fiber in the composite or to the different techniques used to measure the crystallinity such as Wide Angle X-ray Diffraction (WAXS) [19] and DSC [18,20].

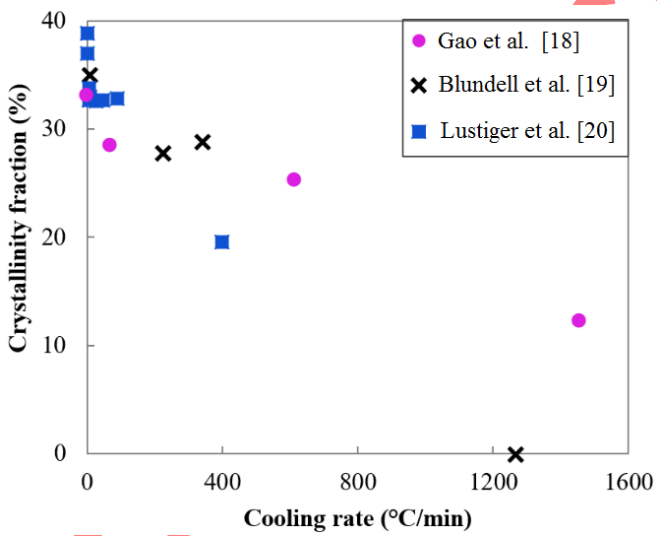

***Figure 4**- Crystallinity fraction for PEEK/AS4 composites function of cooling rate from Gao et al.* [18]*, Blundell et al.* [19] *and Lustiger et al.* [20].

2nd Heating

During second heating, a double endothermic peak appears, indicating the fusion of the crystalline structure. According to the literature [16,21], the first small peak is attributed to the fusion of small crystalline lamellae formed during slow or isothermal crystallization. These lamellae may recrystallize during further heating and form more stable and thicker lamellae. The second peak corresponds to the fusion of thick lamellae which were already present in the specimen together with the ones obtained during the recrystallization of thin lamellae. These two peaks were considered when calculating the overall crystallinity obtained during the slow cooling. It appears that the crystallinity fraction increases during the 2nd heating cycle to 33% ±1.3%. Therefore, it can be concluded that the annealing effect isn't negligible and leads to an increase of around 10% of the crystallinity fraction, reaching the announced maximum crystallinity for PEEK matrix (i.e. 34%). Finally, the crystallinity fraction calculated from DSC scan can be considered as a mean value since it represents the crystallinity of the whole specimen. In fact, the exothermic cold crystallization indicates that a part of the specimens didn't fully crystallize during the process.

3.1.2 Glass transition

The 6 plies and 9 plies UD specimens present a T_g of respectively 140±1.7°C and 141±0.5°C during the 1st heating. T_g increases to 148 ±1.2°C and 148±0.7°C during the 2nd heating for the 6 plies and 9 plies UD specimens, respectively. The values presented here are in accordance with the ones from the literature for PEEK/AS4 and pure PEEK which range between 140.4 and 152°C [22,23].

The shift of T_g by 8°C between the 1st and 2nd heating is in accordance with a previous work on pure PEEK 380G [22]. The DSC tests performed by Atkinson et al. [22] revealed a T_g of 145°C and 152°C for the amorphous and semi-crystalline specimen, respectively.

3.2 Mechanical behavior

3.2.1 *Transverse elastic modulus from static three-point bending tests*

Figure 5 presents the results of the static three-point bending tests of the UD specimens with 6 plies (**Figure 5-(a)**) and 9 plies (**Figure 5-(b)**). The different specimens show a similar trend: an increase in the load with increasing the displacement until the failure followed by a sudden drop in the load.

The flexural moduli are 6.5±0.32 GPa and 6.1±0.6 GPa for the 6 and 9 plies UD specimens, respectively. The differences between the moduli may be due to measurement inaccuracies and/or defects present in the specimen prior to the measurement. Therefore, the results show little dependency of the measured modulus on the thickness i.e. the number of layers (the comparison is made between 6 and 9 plies). As previously stated, the values of the modulus from the static three-point bending tests were used to calibrate the results of the DMA tests presented in the following section.

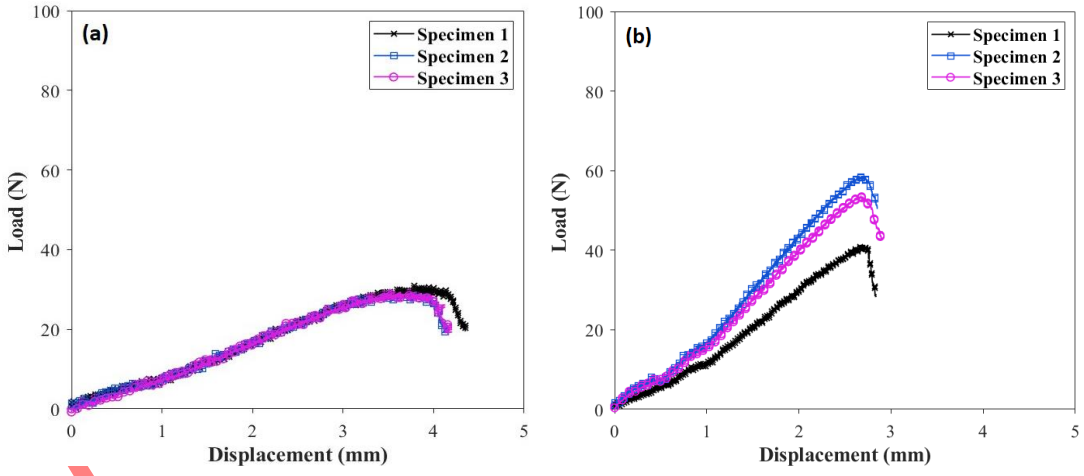

***Figure 5** - Load-displacement curves for different samples in three-point bending tests for the 6 plies (a) and 9 plies (b) UD specimens.*

3.2.2 Thermomechanical behavior of unidirectional laminates: Results of the DMA tests

The variation of the transverse storage modulus E_{22} and the damping factor $tan\,\delta$ with temperature are obtained from the DMA scans. **Figure 6** shows the evolution of E_{22} for the unidirectional specimen manufactured using the cold mandrel during the first heating and the second heating on the DMA test. The results obtained from the work of Unger and Hansen [24] are also presented for the sake of comparison. The

specimen extracted from the same plate behave similarly, so only one specimen for each case is presented in **Figure 6**.

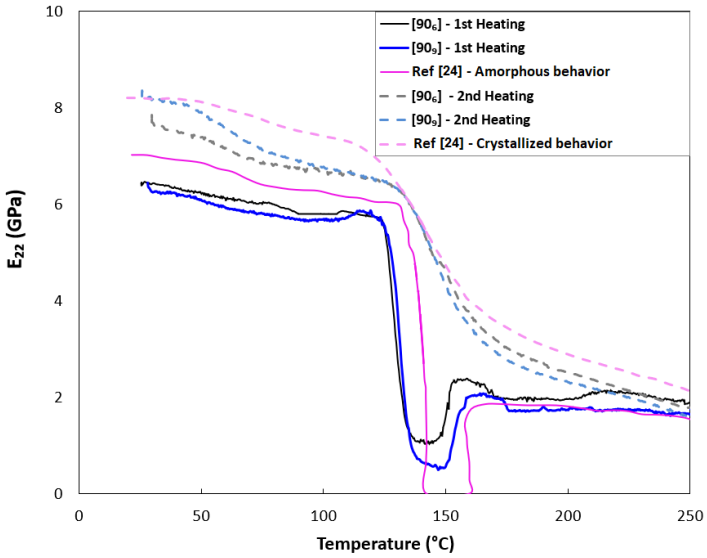

***Figure 6** - Variation of the storage modulus with temperature from DMA tests for the specimens.*

Table 3 lists the maximum standard errors corresponding to the standard deviation maximum values divided by the square root of the specimens' number and the corresponding temperature at which this maximum error occurs for the different specimens. The maximum standard error takes place at ambient temperature for the two laminate sequences and also at 165°C for the 6 plies UD respectively. The maximum value is 15% and can be due to dimensional differences between the different specimens. However, the errors are considered acceptable and the specimens with the same laminate sequence present the same evolution of their modulus with the temperature.

Laminate sequence	Standard error	Temperature (°C)
$[90_6]$	12%	30°C,165°C
$[90_9]$	15%	31°C

***Table 3** – Maximum standard error and the corresponding temperatures for DMA tests.*

During the 1st heating, the transverse modulus for the $[90_6]$ specimen is 6.25 GPa, it slightly decreases to 5.75 GPa at 120°C prior to the glass transition. A barely constant modulus upon heating in the glassy state (below T_g) can be therefore attributed to the specimen under study. Above the glass transition temperature i.e. in the rubbery state, the storage modulus is three times lower than the one in the glassy state. However, it remains almost constant and close to 2 GPa above 190°C ($T_g + 60°C$) until 250°C. The same observation can be made for the $[90_9]$ specimen.

During the glass transition phase of the 1st heating, the specimens' modulus presents an abrupt and sudden decrease as depicted in **Figure 6**. It reaches 1.1 GPa and 0.5 GPa for the 6-plies and 9-plies UD specimen respectively. Upon further heating, the modulus re-increases with temperature and reaches 2 GPa. The modulus increase after the sudden drop occurs within the same temperature range as the exothermal cold crystallization recorded with the DSC tests in the previous part c.f. **Figure 3**. The increase in the modulus can therefore be attributed to the increase in the crystallinity during the cold crystallization. This behavior

was observed for amorphous APC-2 after quenching in [24–26].While the specimen behaves similarly to an amorphous material during the glass transition as it was presented by Unger and Hansen [24], the results of the DSC tests on specimen extracted from the same plates don't suggest a completely amorphous material (the crystallinities were estimated between 19 and 21 %). In light of this, the material under study can be considered as a combination between an amorphous part inducing the behavior observed during the glass transition and a semi-crystalline part for which the presence is highlighted through the DSC results. Therefore, a crystallinity gradient may be present through the thickness of the material which can be the direct result of the thermal history during processing with the unheated mandrel associated with local heating and fast cooling rates. During the second heating, the annealed specimens, i.e. after cooling from 250°C, behave as an APC-2 composite with a semi-crystalline resin. The modulus decreases gradually during the glass transition. After this decrease and until 250°C, E_{22} remains close to 2 GPa which corresponds to 1/3 of the modulus below the glass transition. This behavior is typically observed in literature for APC-2 with a semi-crystalline resin [24–26].

In addition to the transverse modulus, the glass transition temperature T_g can be exploited from the variation of the damping factor $tan\ \delta$ with temperature as discussed in the previous chapter. The glass transition temperatures correspond to the peak of $tan\ \delta$ and are labelled in **Figure 7-(a)** for the 6-plies and **(b)** for the 9-plies UD specimens. The glass transition measured during the 1st heating run ranges between 133 and 136°C according to the DMA tests. It increases to 152°C during the second heating.

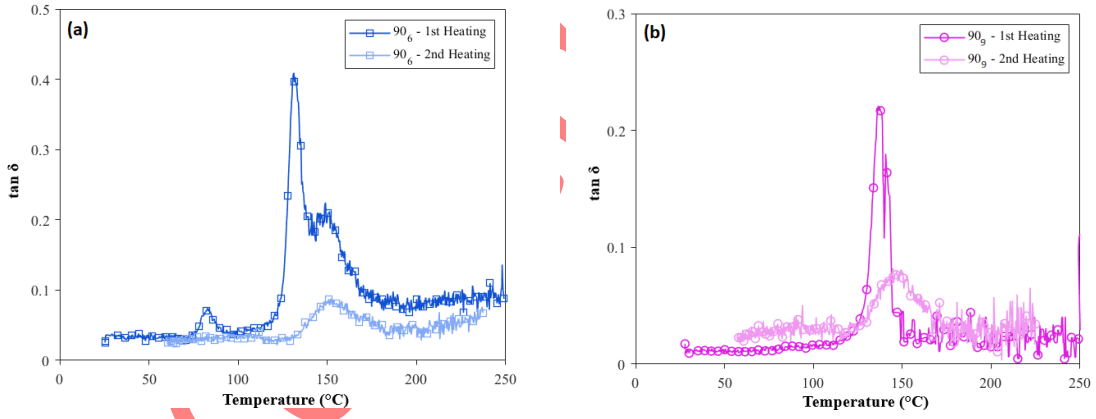

***Figure 7**- Loss factor tan δ function of temperature measured during DMA tests on specimens with (a)- 6 plies & (b)- 9 plies during the first and the second heating.*

For the 1st heating and during the glass transition, a 1st peak is detected, from which the glass transition temperatures have been deduced. This peak is associated with the breaking of the Van Der Waal bonds in the amorphous part of the resin. It is however followed by another one, smaller in intensity which can be clearly detected for the $[90_6]$ laminates in **Figure 7-(a).** This peak is associated with the effect of the recrystallization which takes place during the cold crystallization. The same observation with double peaks was also reported by Cortes et al. [27] when plotting the loss modulus G' vs. temperature for amorphous PEKK. The authors attributed the second peak to the effect of recrystallization. The variation of the glass transition with the increase in crystallinity due to cold crystallization (regardless of the conditions of annealing) are similar to the trends measured with the DSC tests. During the second heating, the peak occurs at a higher temperature, which is correlated with the results obtained from DSC, and the peak intensity is

lower which demonstrates that the amorphous phase is less important compared to the first heating, suggesting that the crystallinity has changed during this second heating.

4 Numerical modelling

The DSC and DMA results presented earlier emphasized the possible presence of a crystallinity gradient through the specimens' thicknesses. To confirm that, a numerical modelling of this gradient through thermal, crystallization and melting models is proposed. The evolution of the crystallinity during the process is directly related to the thermal history applied to the laminate. Therefore, the numerical work is divided into two parts: the first one deals with the thermal modelling of the process followed by a second part where the crystallinity evolution is simulated. The MATLAB computing environment is used for the implementation of the three models described in the following parts.

4.1 Thermal modelling

The thermal modelling approach was adapted from the work of Barasinski [3] and Perez et al. [28] for modelling the tape placement process. The corresponding details can be found in the cited works and a brief description is presented here. First, a geometrical description of the problem is set, including the characteristics of the laser (position relative to the incoming tape and substrate, orientation according to the horizontal plane, divergence and irradiation window size), of the incoming tape (thickness, width and feeding angle), of the substrate (geometry, dimensions and number of plies already deposited) and of the roller (radius). The laser is considered to emit a homogeneous irradiation profile, with a top-hat distribution on the whole window. This study focuses on the manufacturing of plane composite plates. Considering the incident angle of the laser with the material, the orientation of the incoming tape and the material reflectance behavior at the laser wavelength, the laser irradiation is considered to be fully absorbed by the material surface. Only the direct absorption of the laser power is accounted for in the model, the different reflections being neglected. This leads to a uniform distribution of the heat flux density on the tape and the substrate, as was proposed by previous studies (see for example [29]). This heat flux density φ_{rad} is then considered as a boundary condition in the heat problem, as described later. The objective of the thermal model is then to obtain the steady state temperature in a coordinate system attached to the placement head, which is assumed to move with a constant velocity. For a given number of plies, this temperature field can be used to reconstruct the thermal history in any material point. In these conditions, each material point experiences the same thermal history during the process. It is progressively heated when approaching the laser, it reaches its maximum temperature when the laser applies directly on it and it cools down relatively fast when getting far from the heat source, reaching ambient temperature before the next pass when placing the next layer. As a consequence, the laser and the roller are kept fixed and the material is assumed moving with a speed v_{dep} in the opposite direction to the one of the laser and compression head.

In the material domain, consisting in the substrate (i.e. the already placed plies) and the incoming layer, defining the domain $\Omega = [0, L_x] \times [0, L_y]$, as depicted in **Figure 8**, the heat problem (5.1) is solved. This latter is widely considered when modelling ATP processes [3–6,28,30].

$$\begin{cases} \rho C_p\left(\mathbf{v_{dep}}.\boldsymbol{\nabla}T\right) = \boldsymbol{\nabla}.(\mathbf{K}\boldsymbol{\nabla}T), & in\ \Omega \\ (-\mathbf{K}\boldsymbol{\nabla}T).\mathbf{n} = h_{Comp-Air}(T_{amb} - T) + \varphi_{rad}, & on\ \Gamma_{Rad} \\ (-\mathbf{K}\boldsymbol{\nabla}T).\mathbf{n} = h_{Comp-Air}(T_{amb} - T), & on\ \Gamma_{Air} \\ (-\mathbf{K}\boldsymbol{\nabla}T).\mathbf{n} = h_{Comp-Roller}(T_{Roller} - T), & on\ \Gamma_{Roller} \\ (-\mathbf{K}\boldsymbol{\nabla}T).\mathbf{n} = h_{Comp-Tool}(T_{Tool} - T), & on\ \Gamma_{Tool} \\ T = T_{amb}, & on\ \Gamma_{Income} \\ (-\mathbf{K}\boldsymbol{\nabla}T).\mathbf{n} = 0, & on\ \Gamma_{Outcome} \end{cases} \quad (5)$$

ρ, C_p, **K** and T are the material effective density, specific heat, thermal conductivity tensor and temperature respectively. Their values are presented in **Table 4** along with the selected process parameters. All the surfaces in contact with the ambient air, which include Γ_{Rad} and Γ_{Air}, are submitted to a convective heat flux as described in (5.2) and (5.3), respectively. In both cases, $h_{Comp-Air}$ is the convection coefficient between the composite and the ambient environment, which value is given in **Table 4**. The boundary condition also includes the heat flux density from the laser irradiation φ_{rad} on Γ_{Rad}. Thermal contact with the roller and the tool are considered through a convective condition described by (5.4) and (5.5), respectively, where $h_{Comp-Roller}$ and $h_{Comp-Tool}$ are the convection coefficients considered between the composite and the roller or the tool, respectively, and T_{Roller} and T_{Tool} are the prescribed temperatures of the roller and the tool, respectively. They are both considered as constant and equal to T_{Amb}. Values of the convection coefficients are presented in **Table 4**. Finally, it is assumed that the boundary representing the incoming material is at the ambient temperature (5.6), whereas at the opposite boundary the material leaves the domain with a stabilized and uniform temperature field and consequently a null heat flux (5.7).

The heat problem inside the material described in (5) is solved in a Eulerian frame with a fixed roller, laser and deposition head while the material is considered moving at a constant velocity $\boldsymbol{v_{dep}}$. (5) is solved in 2-D for a laminate with N plies. The crystallization enthalpy isn't taken into account in the model since it's negligible compared to the laser heat input [31,32]. The heat problem was solved using the Proper Generalized Decomposition (PGD) method. The resulting solution is the temperature distribution along the length (i.e. along the deposition direction) and through the thickness of a laminate during the deposition of the final ply. For more details on the PGD and the resolution scheme, the reader may refer to [3,28,33].

Property		Unit	Reference	Value
$h_{Comp-Air}$		$(W.m^{-2}.K^{-1})$	[28]	10
$h_{Comp-Roller}$		$(W.m^{-2}.K^{-1})$	[28]	200
$h_{Comp-Tool}$		$(W.m^{-2}.K^{-1})$	[28]	200
$\mathbf{K} = \begin{bmatrix} K_L & 0 \\ 0 & K_T \end{bmatrix}$:	K_L	$(W.m^{-1}.K^{-1})$	[30,34]	4.6
	K_T	$(W.m^{-1}.K^{-1})$	[30,34]	0.43
ρ		$(kg.m^{-3})$	[30]	$\rho = -0.26 \times T + 1619.4$
C_p		$(J.kg^{-1}.K^{-1})$	[30]	$C_p = 4.49 \times T + 593$
Input Power		(W)		1000
v_{dep}		$(m.s^{-1})$		0.15

Table 4 *– Input parameters and properties for the thermal model.*

In this work, the simulated laminate can contain from 1 to 6 plies. The whole domain has a length of 1 m and is discretized with 1500 elements and a thickness of 0.15*n mm with 'n' equal to the ply number in each simulation. Each ply is divided into 10 elements through its thickness. It leads to 11 nodes numbered from 1 to 11 from the bottom to the top i.e. the 1st one (Node 1) is the closest to the mandrel as presented in **Figure 8**.

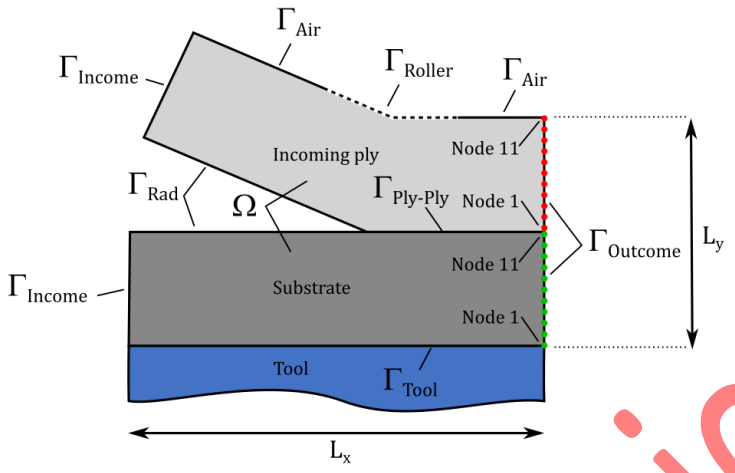

Figure 8 *– Schematic presentation of the problem boundaries and nodes through the thickness of a ply.*

The model presented here was already applied to the study of SPIDE-TP in a previous study [28] and was validated by comparing the temperature field obtained thanks to the model with temperature measured on the irradiated surfaces of the tape and substrate prior contact with an IR camera. The measured and predicted temperature fields presented less than 10°C differences, which demonstrated the robustness of the model.

4.1.1 Predicted thermal history

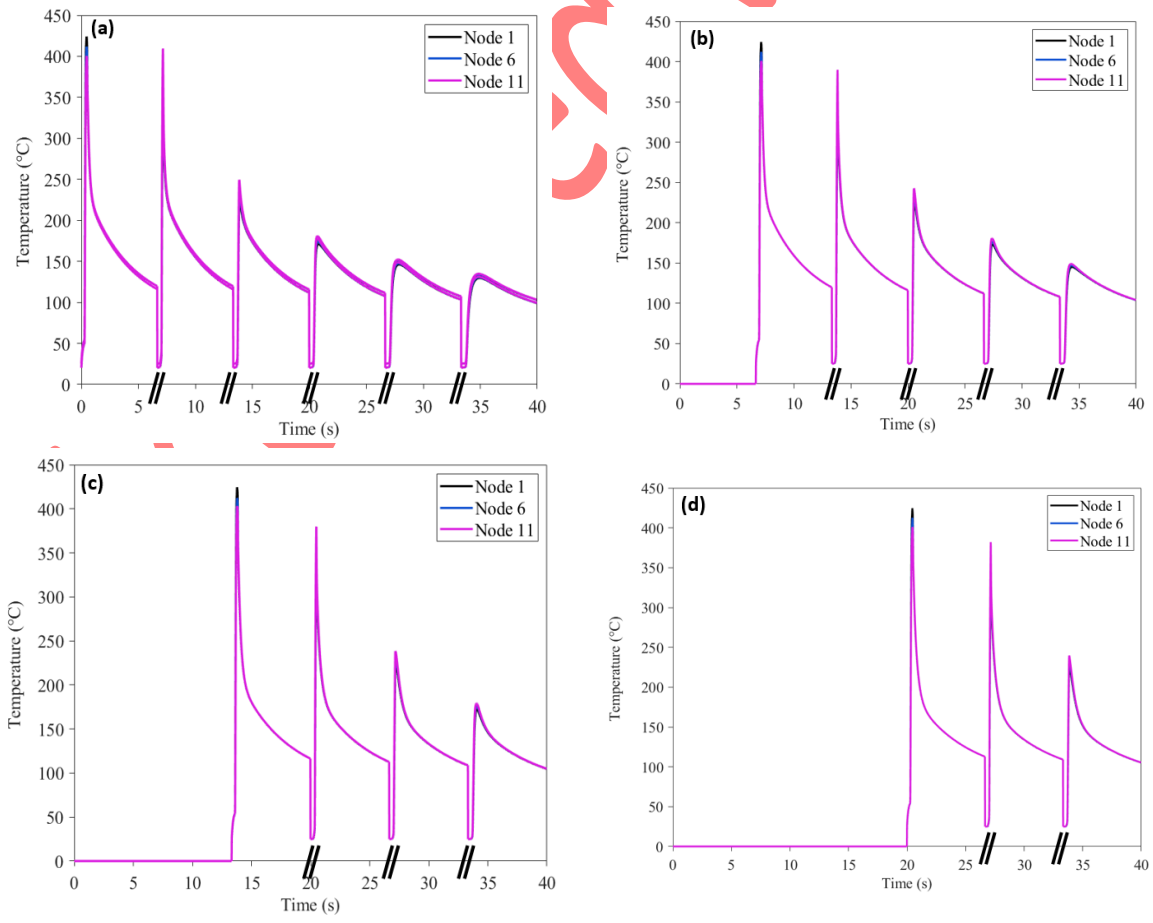

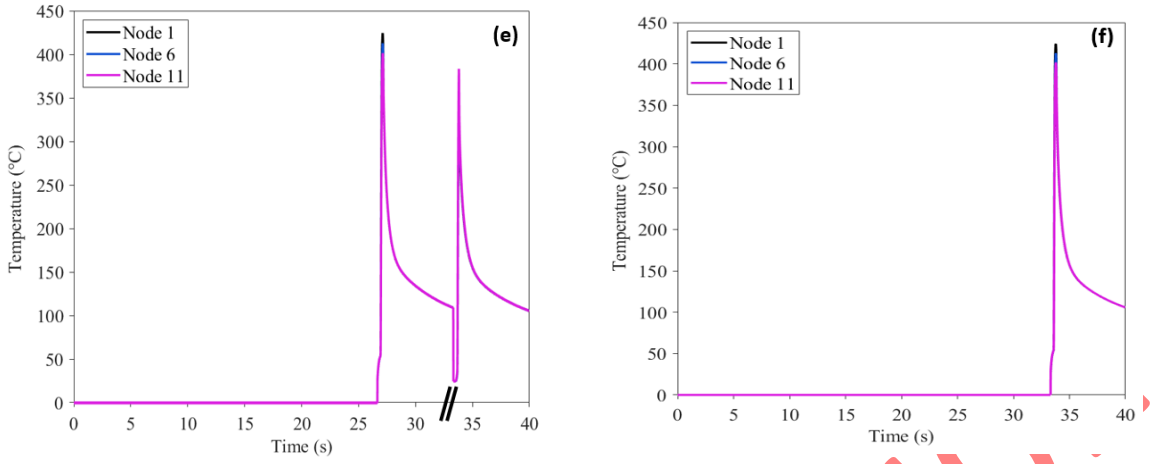

Figure 9 *- Evolution of the temperature with time during the manufacturing of 6 plies laminate for the nodes located at the bottom, the midplane and the surface of (a)- Ply 1, (b)- Ply 2, (c)- Ply 3, (d)- Ply 4, (e)- Ply 5 & (f)- Ply 6 using the PGD solved model.*

The results presented in **Figure 9** show that the different plies behave similarly during the process with a time delay according to their deposition. The maximum temperature differences are related to the temperature during the second peak for the different plies. In order to simplify the description, the temperature evolution of only one ply is detailed in the following. The 3rd ply is chosen c.f. **Figure 10** to omit any boundary effects and a similar description applies for the remaining plies. A sudden drop to 25°C is considered at the end of the deposition in order to limit the simulation time which is symbolized by the symbol // in **Figure 9** and **Figure 10**. In reality, the time is much higher. However, the hypothetical value added isn't supposed to affect the results presented afterwards since the crystallization and the melting occur at temperatures above the glass transition, therefore the cooling rate below this temperature is insignificant to the results.

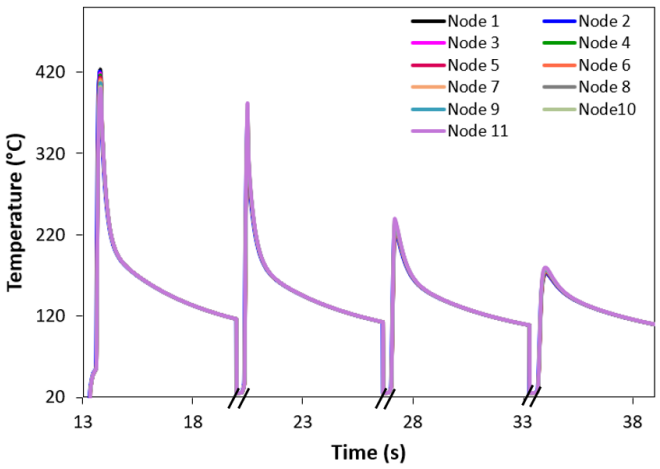

Figure 10 *- Evolution of the temperature with time during the manufacturing of 6 plies laminate for the nodes located at the bottom, the midplane and the surface of Ply number 3 out of 6 plies.*

The evolution of the temperature through the nodes of Ply 3 is presented in **Figure 10**. The deposition of Ply 3 on top of the substrate made from Ply 1 and Ply 2 occurs in the time interval [13.3 s: 19.9 s]. As the ply approaches the laser i.e. between 13.3s and 13.8s, the temperature through the thickness increases and reaches its maximum when the ply is directly subjected to the laser c.f. **Figure 11**-(a). The different nodes

of the ply are heated above the PEEK's documented fusion temperature T_{fusion}=343°C [5]. A temperature gradient is observed during the heating phase with a difference of 25°C between Node 1 and 11 c.f. **Figure 11-(a)**. As the material flows away from the laser, it starts to cool down and the nodes' temperatures gradually decrease. The trends observed for the different nodes are similar to previously reported data on the tape placement of PEEK/AS4 composites [5,6,30].

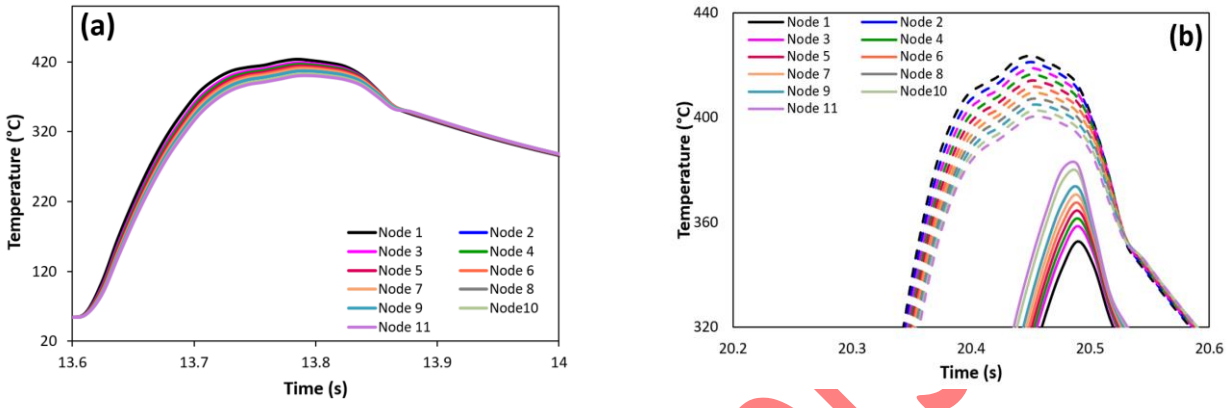

Figure 11 *– Zoom on the temperature profiles from Figure 10 to observe in (a) thermal gradients through the thickness of ply 3 during its deposition & (b) thermal gradient through the thickness of ply 3 (continuous lines) and ply 4 (dashed lines) during the deposition of ply 4 on top of ply 3.*

Once the deposition of ply 3 on the mandrel is completed, ply 4 starts to be placed on top of it which corresponds to the 2nd peak in **Figure 10**. The top surface of Ply 3 (node 11) and the bottom surface of Ply 4 (node 1) are directly exposed to the laser beam. The nodes temperatures of both plies exceed the PEEK's melting temperature of 343°C c.f. **Figure 11-(b)**. The maximum temperatures reached by the tape and the substrate at the interfaces, i.e. Node 1 for Ply 4 and Node 11 for Ply 3, are 424 °C and 410°C respectively. The substrate maximum temperature is reached after the contact between the two surfaces which is evident since the incoming tape is at a higher temperature therefore increasing that of the substrate through conduction when they are in contact. The substrate and the incoming ply surfaces which are in contact do not have the same temperature directly. This is due to the presence of a thermal contact resistance reflecting the intimate contact degree between the plies.

4.2 Crystallization and melting modelling

The initial crystallinity of the incoming ply is considered equal to 0.34 according to the manufacturer description. The evolution of the material crystallinity during the process is simulated using two different models: a crystallization model developed by Choe and Lee [13] which is active below the melting temperature (T_m=343°C), and a melting model proposed by Maffezolli et al. [14] above the melting temperature. The temperature profiles obtained from the PGD solved model are used as input to the melting and crystallization models.

Choe and Lee [13] developed a model for the non-isothermal crystallization where the crystallization of PEEK is presented as a combination of two nucleation-growth mechanisms [35]. The expression derived is based on Tobin's theory of phase transition kinetics. The crystallinity fraction X_t at time t can be obtained using Equation (6). Details on the equations and the parameters used can be found in the cited reference [13]. The crystallization model is applied during heating and cooling between T_m (343°C) and T_g (143°C).

$$\frac{d\alpha(t)}{dt} = \kappa_1 \exp\left(-\frac{3E_d}{RT}\right) exp\left(-\frac{3\Psi_1 T_m^0}{T(T_m^0 - T)}\right) t^2[1-\alpha(t)]^2 + \kappa_2 exp\left(-\frac{3E_d}{RT}\right) exp\left(-\frac{(3\Psi_1 + \Psi_2)T_m^0}{T(T_m^0 - T)}\right) \times [1-\alpha(t)]^2 \int_0^t (t-w)^2[1-\alpha(w)]dw \quad (6)$$

T_m^0, E_d, Ψ_1 and Ψ_2 are respectively the equilibrium melting temperature, the activation energy of diffusion of crystallization segments across the phase boundary, the constant related to the free energy of formation of a critical nucleus and the constant related to the free energy of formation of a growth embryo. κ_1 and κ_2 are kinematic parameters. $\dot{\alpha}(t)$ presents the rate of variation of the relative crystallinity $\alpha(t) = X_t(t)/X_\infty(t)$ at time t with $X_t(t)$ and $X_\infty(t)$ are the volume fraction crystallinity and the ultimate volume fraction crystallinity at time t. The values for the different parameters were obtained by Choe and Lee [13] through DSC measurements. The crystallization model is applied during heating and cooling between $T_m(343°C)$ and $T_g(143°C)$.

In this study, the melting kinetics are based on Maffezolli et al.'s model [14]. It was initially applied to the resistance welding process and later used by several authors during the tape placement [6,12,36]. It is based on integrating the rate of heat absorbed during the melting process using Equation (7).

$$X_t(t) = X_t(t_{in})\left(1 - 0.5\int_{t_{in}}^{t} K_A dt\right)^2 \quad (7)$$

t_{in} and $X_t(t_{in})$ correspond to the time and the crystallinity fraction obtained when the material reaches 320°C during heating, the value considered by Maffezolli et al. at which the melting of the crystals begins. K_A is a factor obtained using a relation between the activation energy, the universal gas constant and a pre-exponential factor which are detailed in [14].

4.2.1 Predicted crystallinity evolution

As in the case of the temperature history, the behavior of the 3rd ply nodes is described and it can be applied to the remaining plies. The temperature history and the corresponding melting behavior for nodes 1 to 11 of Ply 3 during its deposition are presented in **Figure 12-(a).**

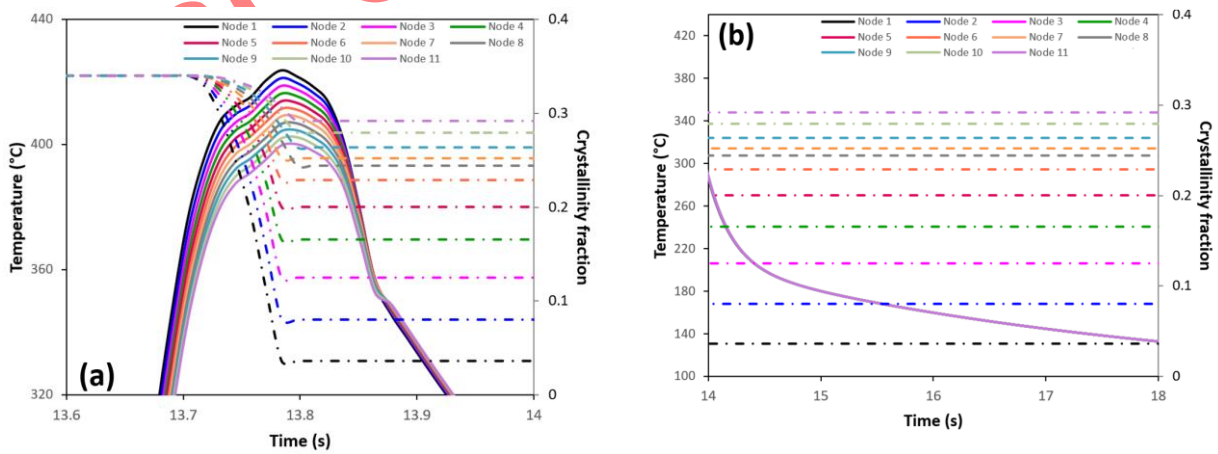

Figure 12-*Evolution of the temperature and crystallinity fraction for the different nodes of Ply 3 during its deposition. Continuous lines (-) present the temperature while dashed lines (-.-) present the crystallinity.*

The maximum temperature is 421°C for Node 1 directly exposed to the laser source with a difference of 22°C with Node 11 located at the other side from the laser with a temperature around 399°C. While all the nodes are heated above the melting temperature, the melting model predicts a gradient in the residual crystallinity. For instance, Node 11 has a residual crystallinity of 26% compared to a negligible (less than 3%) crystallinity for Node 1. The melting behavior is related to the temperature and the time spent at this temperature: the higher the temperature and time spent, the higher the melted crystals fraction. The melting of crystals is followed by their crystallization during the cooling from 320°C which is presented in **Figure 12**-(b). The increase in the crystallinity in Ply 3 is negligible and this directly results from the high cooling rates obtained through the thermal model. The cooling rates are high (up to 2200°C/s) which leads to insufficient time for the crystallization to occur.

On the other hand, during the deposition of Ply 4 on top of Ply 3, the different nodes of Ply 3 are reheated above PEEK's fusion temperature but at lower temperatures compared to the ones presented in **Figure 12**. The melting model predicts a re-melting of the different nodes. It can be seen in **Figure 13-(a)** that the crystallinities of nodes 8 to 11 (11 being the closest to the laser) decrease more importantly than nodes 1 to 7. For example, the crystallinity of Node 11 decreases from 27 % at the end of the placement of Ply 3 to 24% during the reheating of Ply 3 when Ply 4 is deposited. The crystallinity fractions of different nodes increase again during their cooling (**Figure 13-(b))** however this increase remains negligible due to the high cooling rates (a maximum increase of 0.05% at Node 11).

During the deposition of Ply 3, the maximum temperature reached through the thickness of Ply 1 is 248°C (at Node 11) which is lower than the PEEK's melting temperature so no re-melting occurs through the thickness of Ply 1. On the other hand, a re-crystallization phenomenon takes place since the nodes are heated above their glass transition with a very negligible increase compared to the crystallinity fraction once the deposition of the 1st ply is achieved.

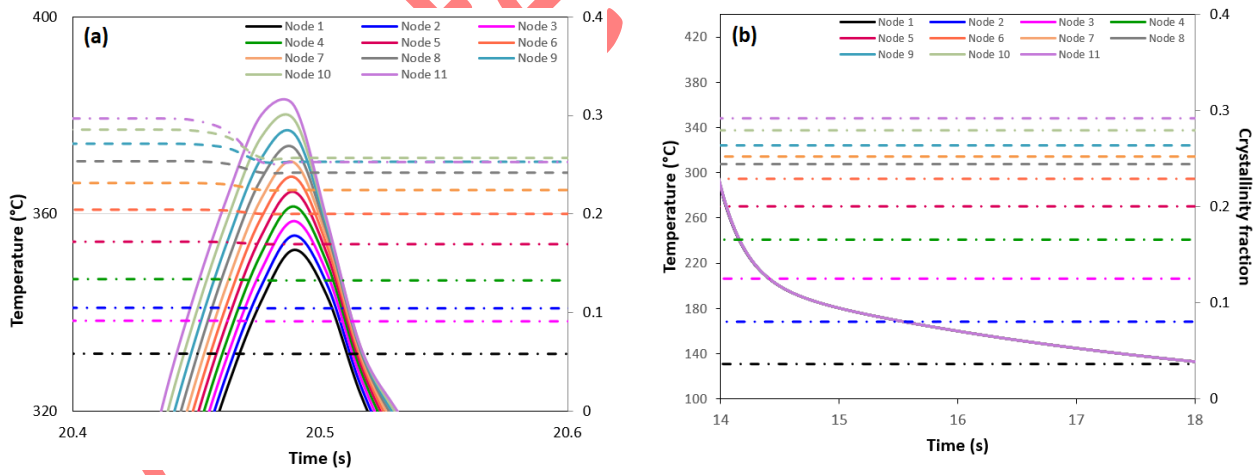

Figure 13 *-Evolution of the temperature and crystallinity fraction for the different nodes of Ply 3 during the heating (a) and cooling (b) phases when Ply 4 is being placed. Continuous lines (-) present the temperature while dashed lines (-.-) present the crystallinity.*

It can be concluded that the model predicts that the crystallinity fraction through the thickness of a ply 'n' is mainly established during its deposition. Small changes may be induced due to the re-melting during the deposition of the next ply 'n+1' and this effect disappears once the ply 'n+2' starts to be placed. The crystallinities may be slightly increased during the deposition of the remaining plies since the plies can be

reheated above their glass transition temperature. However, the contribution of the crystallization during cooling to the final crystallinity is negligible and this is directly related to the high cooling rates.
Finally, the crystallinity fractions through the thicknesses of the different plies predicted by this model are presented in **Figure 14**. The results show a similar behavior for all the plies. The differences in terms of crystallinity values are possibly due to the different number of reheating and re-cooling phases to which each ply is subjected or the maximum temperature differences between the plies predicted by the thermal model**.**

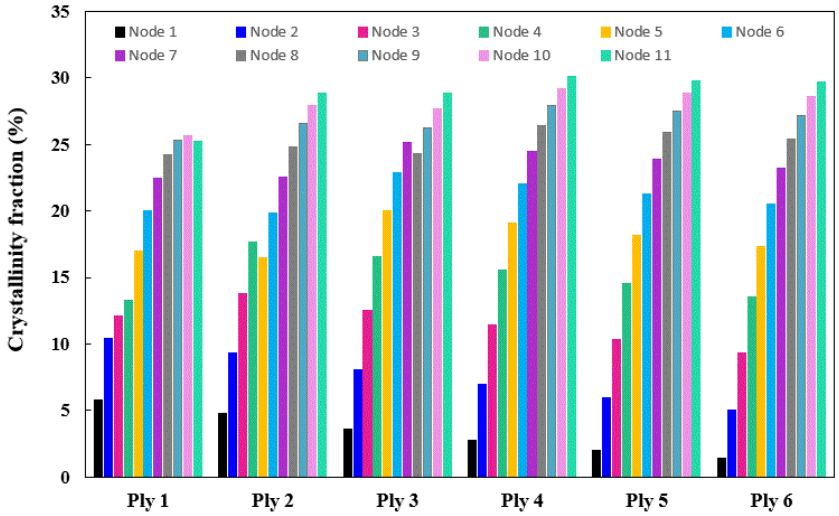

Figure 14 *– Predicted crystallinity fractions through the thickness of the six plies at the end of the process.*

The model predicts the presence of a crystallinity gradient through each ply thickness and through the substrate thickness. A layer exists between every two consecutive plies presenting a lower crystallinity than the rest of the ply's thickness (<5%). The crystallinity fraction is in general maximum at Node 11 for each ply. In order to characterize the crystallinity gradient through the thickness using DSC scans, a rigorous work should be conducted to perform precise cuts through the laminate thickness without modifying the material crystallinity. This work was hard to perform using the current material but will be the subject of future studies. However, the simulated average crystallinity overall the laminate thickness can be compared to that measured using DSC. The modeled average crystallinity through the thickness of the different nodes is 19.7% which is close to the 23.5% value measured for the 6-plies laminates using DSC. The difference is 1.6% which can be accepted within the scope of the errors from the model and the measurements using DSC.

5 Conclusions and future works.

This study aimed at investigating the presence of crystallinity gradients through the thickness of carbon fibre reinforced PEEK composite structures obtained by laser assisted tape placement. DSC tests were performed to identify the mean crystallinity through the thickness of the produced part. They led to partially crystallized material with a mean value comprised between 21.4% and 23.5% depending on the stacking sequence. This correspond to values lower than the maximum crystallinity fraction for this material which is expected to be 34%. DMA tests under three-point bending led to the evolution of the transverse modulus of the composite material with temperature. The observed behavior was characteristic of an amorphous composite which is incompatible with the crystallinity level observed in DSC. Therefore, the hypothesis of

a material composed of alternative amorphous and semi-crystalline layers was suggested. As these gradients are difficult to identify experimentally, a multi-physical model including heat transfer, crystallization kinetics and fusion kinetics was presented in order to estimate the distribution of crystallinity through the thickness of the composite structure. Results indicate the presence of nearly amorphous layers (around 3% of crystallinity) between every two consecutive plies, when the core of each plies remains at a high crystallinity level. This distribution leads to a mean crystallinity value close to the one obtained by DSC, and would be compatible with the mechanical behavior obtained by DMA. This study therefore permits to indirectly investigate the presence of crystallinity gradients in semi-crystalline thermoplastic composite materials obtained by laser assisted tape placement process. As a consequence, DMA analysis is a powerful tool to investigate the physical and mechanical states of the material after processing. The DMA and DSC results also demonstrated that an annealing at 250°C led to a relative increase in the mean crystallization fraction and transversal modulus by 10% and 20%, respectively. This thermal treatment would benefit to the part stiffness but would also lead to a higher crystallization shrinkage of the material and, therefore, to higher residual stresses levels. Deeper investigations are currently performed to determine if there are optimum deposition parameters and crystallinity distribution to obtain high mechanical properties and low residual stresses.

6 References

[1] Lukaszewicz DH-JA, Ward C, Potter KD. The engineering aspects of automated prepreg layup: History, present and future. Compos Part B Eng 2012;43:997–1009. doi:10.1016/j.compositesb.2011.12.003.

[2] Boon YD, Joshi SC, Bhudolia SK. Review : Filament Winding and Automated Fiber Placement with In Situ Consolidation for Fiber Reinforced Thermoplastic Polymer Composites. Polymers (Basel) 2021;13:1–29.

[3] Barasinski A. Modélisations du procédé de placement de fibres composites à matrice thermoplastique. PhD Thesis, Ecole Centrale de Nantes, Nantes, France, 2012.

[4] Chinesta F, Leygue A, Bognet B, Ghnatios C, Poulhaon F, Bordeu F, et al. First steps towards an advanced simulation of composites manufacturing by automated tape placement. Int J Mater Form 2014;7:81–92. doi:10.1007/s12289-012-1112-9.

[5] Stokes-Griffin CM, Compston P. A combined optical-thermal model for near-infrared laser heating of thermoplastic composites in an automated tape placement process. Compos Part A Appl Sci Manuf 2015;75:104–15. doi:10.1016/j.compositesa.2014.08.006.

[6] Sonmez FO, Hahn HT. Modeling of Heat Transfer and Crystallization in Thermoplastic Composite Tape Placement Process. J Thermoplast Compos Mater 1997;10:198–240. doi:10.1177/089270579701000301.

[7] Wu D, Miao Q, Dai Z, Niu F, Ma G. Effect of voids and crystallinity on the interlaminar shear strength of in-situ manufactured CF/PEEK laminates using repass treatment. Compos Sci Technol 2022;224:109448. doi:10.1016/j.compscitech.2022.109448.

[8] Mantell SC, Springer GS. Manufacturing Process Models for Thermoplastic Composites. J Compos Mater 1992;26:2348–77. doi:10.1177/002199839202601602.

[9] Lee W Il, Springer GS. A Model of the Manufacturing Process of Thermoplastic Matrix Composites. J Compos Mater 1987;21:1017–55. doi:10.1177/002199838702101103.

[10] Velisaris CN, Seferis JC. Crystallization kinetics of polyetheretherketone (peek) matrices. Polym

Eng Sci 1986;26:1574–81. doi:10.1002/pen.760262208.

[11] Nejhad MNG, Gillespie JW, Cope RD. Prediction of Process-Induced Stresses for In-Situ Thermoplastic Filament Winding of Cylinders. Comput. Aided Des. Compos. Mater. Technol. III, Dordrecht: Springer Netherlands; 1992, p. 225–53. doi:10.1007/978-94-011-2874-2_15.

[12] Tierney JJ, Gillespie Jr. JW. Crystallization kinetics behavior of PEEK based composites exposed to high heating and cooling rates. Compos Part A Appl Sci Manuf 2004;35:547–58. doi:10.1016/j.compositesa.2003.12.004.

[13] Choe CR, Lee KH. Nonisothermal crystallization kinetics of poly(etheretherketone) (PEEK). Polym Eng Sci 1989;29:801–5. doi:10.1002/pen.760291208.

[14] Maffezzoli A, Kenny JM, Nicolais L. Welding of PEEK/carbon fiber composite laminates. SAMPE J 1989;25:35–40.

[15] Pérez-Martín H, Mackenzie P, Baidak A, Ó Brádaigh CM, Ray D. Crystallinity studies of PEKK and carbon fibre/PEKK composites: A review. Compos Part B Eng 2021;223:109127. doi:10.1016/j.compositesb.2021.109127.

[16] Blundell DJ, Osborn BN. The morphology of poly(aryl-ether-ether-ketone). Polymer (Guildf) 1983;24:953–8. doi:10.1016/0032-3861(83)90144-1.

[17] ISO. EN ISO 14125:1998 - Fibre-reinforced plastic composites — Determination of flexural properties 1998.

[18] Gao S-L, Kim J-K. Cooling rate influences in carbon fibre/PEEK composites. Part 1. Crystallinity and interface adhesion. Compos Part A Appl Sci Manuf 2000;31:517–30. doi:10.1016/S1359-835X(00)00009-9.

[19] Blundell DJ, Chalmers JM, Mackenzie MW, Gaskin WF. Crystalline morphology of the matrix of PEEK-carbon fiber aromatic polymer composites. I. Assessment of crystallinity. SAMPE Q 1985;16.

[20] Lustiger A, Uralil FS, Newaz GM. Processing and structural optimization of PEEK composites. Polym Compos 1990;11:65–75. doi:10.1002/pc.750110109.

[21] Tardif X, Pignon B, Boyard N, Schmelzer JWP, Sobotka V, Delaunay D, et al. Experimental study of crystallization of PolyEtherEtherKetone (PEEK) over a large temperature range using a nano-calorimeter. Polym Test 2014;36:10–9.

[22] Atkinson J, Hay JN, Jenkins MJ. Enthalpic relaxation in semi-crystalline PEEK. Polymer (Guildf) 2002;43:731–5. doi:10.1016/S0032-3861(01)00668-1.

[23] Borgna T. Etude des proprietes de composites a matrice thermoplastique thermostable au-dela de leur temperature de transition vitreuse. PhD Thesis, Université de Pau et des Pays de l'Adour, Pau, France, 2017.

[24] Unger WJ, Hansen JS. The Effect of Cooling Rate and Annealing on Residual Stress Development in Graphite Fibre Reinforced PEEK Laminates. J Compos Mater 1993;27:108–37. doi:10.1177/002199839302700201.

[25] D'Amore A, Cocchini F, Pompo A, Apicella A, Nicolais L. The effect of physical aging on long-term properties of poly-ether-ketone (PEEK) and PEEK-based composites. J Appl Polym Sci 1990;39:1163–74. doi:10.1002/app.1990.070390511.

[26] Russell JD, Curliss DB. Effects of Thermal History and Jet Fuel Absorption on the Properties of

APC-2. J Thermoplast Compos Mater 1992;5:238–55. doi:10.1177/089270579200500304.

[27] Quiroga Cortés L, Caussé N, Dantras E, Lonjon A, Lacabanne C. Morphology and dynamical mechanical properties of poly ether ketone ketone (PEKK) with meta phenyl links. J Appl Polym Sci 2016;133:n/a-n/a. doi:10.1002/app.43396.

[28] Perez M, Barasinski A, Courtemanche B, Ghnatios C, Chinesta F. Sensitivity thermal analysis in the laser-assisted tape placement process. AIMS Mater Sci 2018;5:1053–72. doi:10.3934/matersci.2018.6.1053.

[29] Weiler T, Emonts M, Wollenburg L, Janssen H. Transient thermal analysis of laser-assisted thermoplastic tape placement at high process speeds by use of analytical solutions. J Thermoplast Compos Mater 2018;31:311–38. doi:10.1177/0892705717697780.

[30] Le Louët V. Etude du comportement thermique de bandes composites pré-imprégnées au cours de procédé de fabrication AFP avec chauffage laser. PhD Thesis, Université de Nantes, Nantes, France, 2018.

[31] Pitchumani R, Ranganathan S, Don RC, Gillespie JW, Lamontia MA. Analysis of transport phenomena governing interfacial bonding and void dynamics during thermoplastic tow-placement. Int J Heat Mass Transf 1996;39:1883–97. doi:10.1016/0017-9310(95)00271-5.

[32] Tierney J, Gillespie JW. Modeling of In Situ Strength Development for the Thermoplastic Composite Tow Placement Process. J Compos Mater 2006;40:1487–506. doi:10.1177/0021998306060162.

[33] Chinesta F, Keunings R, Leygue A. The Proper Generalized Decomposition for Advanced Numerical Simulations. Cham: Springer International Publishing; 2014. doi:10.1007/978-3-319-02865-1.

[34] Cogswell FN. Thermoplastic aromatic polymer composites: a study of the structure, processing, and properties of carbon fibre reinforced polyetheretherketone and related materials. Oxford: Butterworth-Heinemann; 1992.

[35] Keith HD. Crystallization of polymers from the melt and the structure of bulk semicrystalline polymers. Kolloid-Zeitschrift Und Zeitschrift Für Polym 1969;231:421–38. doi:10.1007/BF01500010.

[36] Mantell SC, Springer GS. Thermoplastic composites for aerospace. Reinf Plast 2019;63:14–5. doi:10.1016/j.repl.2018.12.049.